A generalisation of the Hill's quadratic yield function for planar plastic anisotropy to consider loading direction

R.P.R. Cardoso[a,*], O.B. Adetoro[b]

[a] Brunel University London, Uxbridge, UB8 3PH London, UK
[b] University of the West of England, BS16 1QY Bristol, UK

ARTICLE INFO

ABSTRACT

In this work, a new generalised quadratic yield function for plane stress analysis that is able to describe the plastic anisotropy of metals and also the asymmetric behaviour in tension-compression typical of the Hexagonal Closed-Pack (HCP) materials, is developed. The new yield function has a quadratic form in the stress tensor and it simultaneously predicts the r-values and directional flow stresses, which is shown to agree very well with experimental results. It also accurately describes the biaxial symmetric stress state which is fundamental for the accurate modelling of aluminium alloys. The new quadratic yield function represents the non-symmetric biaxial stress state by performing a linear interpolation from pure uniaxial loading to a biaxial symmetric stress state. The main advantages of this new yield function is that it can be used for the modelling of metals with any crystallographic structure (BCC, FCC or HCP), it only has five anisotropic coefficients and also that it is a simple quadratic yield criterion that is able to accurately reproduce the plastic anisotropy of metals whilst using an associated flow rule.

1. Introduction

Material modelling is very important not only for the development of new metal alloys but also for the simulation of manufacturing processes. Within material modelling, plasticity plays a fundamental role and its description is essential for the accurate design of manufacturing processes. In plasticity, yield functions are critical because they provide the yielding point of the material and also when used within an associated flow rule scheme, they describe the plastic flow of the metal accurately. One of the first yield functions for plastic anisotropy was developed in the pioneer work by Hill (1948) [20]. Hill developed a quadratic yield function with anisotropic coefficients that could either predict the r-values or directional flow stresses, but never both simultaneously. Moreover, Hill's original yield function does not include the effect of the biaxial symmetric stress and so it is not accurate in the modelling of aluminium alloys. Many posteriori yield functions [2–6] were developed after Hill's and the coefficients of these yield functions were designed to include the biaxial symmetric stress effect. Whilst the equi-biaxial flow stress has been defined in these functions, none of them have characterised the coefficients for the unsymmetric biaxial stress state between pure uniaxial loading and equi-biaxial loading.

The predominant deformation mechanism in Face-Cubic-Centred metals (FCC) such as aluminium alloys, is deformation by slip in the crystallographic slip systems, which is basically a consequence of the movement of dislocations. In FCC materials, compressive and tensile strengths are virtually identical and yielding is not influenced by the hydrostatic pressure as well. The yield surface of such materials is usually represented adequately by an even function of the principal values of the deviatoric stresses (e.g. Hershey [19] and Hosford [21]). Hexagonal Close-Packed (HCP) materials, such as magnesium and titanium alloys, have less active slip systems at low/room temperatures but they have additional twinning systems that accommodate plastic deformation by a different mechanism known as twinning or distortion of the lattice. Twinning is a polar deformation mechanism (it only develops in one direction) and this is the main reason for the asymmetric behaviour observed on HCP alloys in tension-compression.

For the description of incompressible plastic anisotropy, many yield functions have been suggested based on the isotropic hardening assumption (Hill [20], Barlat and Lian [2], Barlat et al. [3], Karafillis and Boyce [23]). Among them, Cazacu and Barlat [10] introduced a general formulation which originated from the rigorous theory of representation of tensor functions. However with this approach, the conditions for the convexity of the yield surface are difficult to derive and impose. The convexity has a physical basis and, in addition, this property ensures numerical stability in computer simulations. For this reason, a particular case of this general theory, which is based on linearly transformed stress components has received more interest from

the metal forming and material modelling communities in general. Barlat et al. [3] applied this method to a full stress state in an orthotropic material and Karafillis and Boyce [23] generalised it as the so-called isotropic plasticity equivalent theory with a more general yield function and a linear transformation that can accommodate lower material symmetry.

Cazacu et al. [11] proposed a criterion based on a linear transformation that accounts for the strength-differential effect, particularly prominent in Hexagonal Closed-Pack (HCP) materials, with the work being extended in Plunkett et al. [31] and Plunkett et al. [30] by including the effect of texture development in the yield function. Barlat et al. [5,6] later introduced two linear transformations which were applied on the sum of two yield functions in the case of plane and general stress states, in order to improve the accuracy of the functions by Cazacu et al. [11], Plunkett et al. [31] and Plunkett et al. [30] in the modelling of the anisotropic behaviour of aluminium sheets. Bron and Besson [8] further extended Karafillis and Boyce's approach to two linear transformations. These recently proposed yield functions include more anisotropy coefficients and therefore give a better description of the anisotropic properties of a material. Although the mathematical formulations are complex and very heavy from a computational point of view. These reported developments in yield functions have been particularly important for the study of the formability of sheet metals as shown in the works of Kuroda and Tvergaard [25], Stoughton and Yoon [36], Lou et al. [28] and Dasappa et al. [14].

Apart from the phenomenological studies listed above, another approach for the prediction of plastic anisotropy and strain hardening is the one based on polycrystal plasticity models. Commercial aluminium and magnesium alloys such as the aluminium AA6022 and AA2090 and the magnesium AZ31B used in this paper and used generally in forming operations, are polycrystalline materials composed of numerous grains each with a given lattice orientation with respect to macroscopic axes. At low temperatures, metals and alloys deform by dislocation glide or slip on given crystallographic planes and directions thereby producing microscopic shear deformations (Kocks et al. [24]). Therefore, the distribution of grain orientations and crystallographic texture in general, play an important role in the study and in the modelling of plasticity. Due to the geometrical nature of slip deformations, strain incompatibilities usually arise between grains thereby producing micro-residual stresses, which from a macroscopic point of view, can lead to the well-known Bauschinger effect. Slip results in gradual lattice rotation where dislocations accumulate at micro-structural barriers, increasing the slip resistance and consequently strain hardening. There is also another crystallographic deformation mechanism that is very typical of HCP materials which is the twinning. Proust et al. [32] developed the modelling of texture, twinning and hardening evolution of hexagonal materials by using the well-known Visco-Plastic Self-Consistent (VPSC) approach (Lebensohn and Tome [26]), where the interaction between a grain and its surrounding effective medium is taken into account. Polycrystal models can be used in multi-scale simulations of metal forming operations, but they are usually expensive in computational time.

Some noteworthy studies that use dislocation motion, micro-structural grain size and shape data for the prediction of the yield strength of metallic alloys include the studies by Esmaeili et al. [17] and Balogh et al. [1], while some other studies perform a macroscopic study on the anisotropy of aluminium sheets from the consideration of morphological texture and crystallographic texture evolution (Choi et al. [12]). Polycrystal modelling aspects have been treated in a large number of publications and books such as in Kocks et al. [24], Gambin [18] and Dawson [15]. More recently, crystallographic plasticity has been extensively used in several numerical simulations, because it naturally predicts texture evolution and anisotropy, Bauschinger effect, transient behaviour and permanent softening. However, their computational cost is still prohibitive when compared to the use of phenomenological constitutive models.

Most of the early developed phenomenological yield potentials (e.g. von-Mises [38] and Hill's [20]) are quadratic in the stress tensor. These yield potentials were mainly designed from distortion energy balance equations, and they were developed primarily for steel alloys, with Hill's 1948 [20] going a step further by including plastic anisotropy in the potential. It is widely accepted that these potentials fit the yield locus very well for steel, but are unable to accurately predicting the anomalous behaviour of aluminium alloys (Dodd and Caddell [16]), especially in reproducing the yield locus on the vicinity of the symmetric biaxial stress state. There are two ways of accurately model aluminium alloys: i) by using non-quadratic yield functions with associated flow rules; ii) by using quadratic yield functions with non-associated flow rules (Stoughton and Yoon [37]), where in this case a plastic potential needs to be defined for the plastic flow. The use of non-associated flow rules allows for the use of simpler yield potentials, such as the quadratic potential of Hill 1948 [20], but a second plastic potential needs to be used for the plastic flow. The use of two different potentials in the non-associated flow rule can however lead to difficulties during return mapping procedures, especially if the loci of the two potentials (yield and plastic potential) are of considerably different shapes. Considering however the flexibility in phenomenological modelling, it must be possible to develop a quadratic generalised yield function for simultaneously predicting r-values and directional flow stresses accurately as opposed to the individual treatment that has been adopted so far. It also follows to say that it must be possible to simultaneously match the r-values and directional flow stresses for any stress state, as for example under planar anisotropy assumption. This generalised yield function must be able to accurately predict the anomalous aluminium behaviour [16] and the symmetric biaxial stress state. Certainly, the yield function must be accurate for a wide range of cases and valid if, and only if, it is proven to be convex in the principal stress space. Therefore, the main ideas for the new yield function proposed in this paper are as follows:

- A new quadratic yield function is developed for the simultaneous prediction of r-values and directional flow stresses and its convexity is proven in Appendix A for the case of proportional loading;
- This new model can simultaneously predict the r-values and directional flow stress accurately for any given angle from the rolling direction;
- The biaxial symmetric flow stress is incorporated in this new quadratic yield function (this is detailed in Section 2.1). However, the biaxial r-value is not included in this formulation;
- It is postulated that the stress tensor changes in a linear manner between symmetric biaxial stress state and unaxial stress state, hence it is included in the new quadratic yield function in an interpolatory manner (details given in Section 2.1);
- Consequently due to this new quadratic yield function, it is possible to simultaneous predict r-values and directional flow stress from the use of an associated flow rule;

The main objective of this research work is therefore to develop the yield function for plane stress analysis as general as possible so that it can work with associated flow rules for the modelling of planar anisotropy for both FCC and HCP materials and also that it is able to describe the asymmetric behaviour in tension-compression typical of HCP materials.

2. Model formulation

In this formulation, the well-established Hill's [20] yield potential is used and extra flexibility is introduced in some coefficients in order to achieve a fully generalised function. Hill [20] proposed a yield function that can be used for the study of the planar anisotropy of metals and for which the equivalent stress is defined as:

$$\bar{\sigma} = \sqrt{\frac{3}{2}} \sqrt{\frac{(G+H)\sigma_{xx}^2 + (F+H)\sigma_{yy}^2 - 2H\sigma_{xx}\sigma_{yy} + 2N\tau_{xy}^2}{F+G+H}} \tag{1}$$

The coefficients F, G, H and N are designed to fit the r-values or, alternatively, the directional flow stresses but never both in simultaneous. This is a major limitation in Hill's yield potential because both fitting is required for the accurate modelling of planar plastic anisotropic metals. Hill's yield potential has however some great advantages which are its quadratic form and the simplicity of the model for the description of plastic anisotropy.

Therefore, a new yield function (YldParam) is defined as:

$$\bar{\sigma} = \frac{1}{C_a(u)} \sqrt{\frac{3}{2}} \sqrt{\frac{(G+H)\sigma_{xx}^2 + [F(u)+H]\sigma_{yy}^2 - 2H\sigma_{xx}\sigma_{yy} + 2N\tau_{xy}^2}{F(u)+G+H}} \tag{2}$$

where $C_a(u)$ is a new coefficient which defines the anisotropy in the yield stresses and the anisotropy for the r-values is conserved from the adaptation of coefficient F from the original Hill's model by making it variable. Both coefficients are a function of a parametric coordinate u, which represents the orientation of the loading direction when measured from the rolling direction. This parametric variable u exists within the limits $0.0 \leq u \leq 1.0$, with $u = 0.0$ defining the rolling direction, $u = 0.125$ being 45° from the rolling direction, $u = 0.25$ defining 90° with the rolling direction and finally $u = 1.0$ again defining the rolling direction. The coefficient $C_a(u)$ is designed to fit the yield stresses while the coefficient $F(u)$ is designed to fit the r-values. In this work, the functions for these two anisotropic coefficients are described from the use of Non-Uniform Rational B-Splines (NURBS) but they can also be described from the use of any other type of functions as far as the accurate values for the coefficients are conserved. The main reasons for the use of NURBS are essentially related to the local compact support of NURBS which is explained in more detail later in this manuscript. It is also demonstrated in Appendix A that the new yield potential for plane stress analysis delivers a convex yield locus, which is a fundamental prerequisite for a stable stress integration procedure in elasto-plastic material modelling. The Hill's coefficients H, G and N are obtained from the experimental r-values at 0°, 45° and 90° from the rolling direction [20]:

$$H = \frac{2r_0}{1+r_0}$$
$$G = \frac{2}{1+r_0}$$
$$N = \frac{2(r_0+r_{90})(2r_{45}+1)}{2r_{90}(1+r_0)} \tag{3}$$

The r-value anisotropic coefficient $F(u)$ will be calculated from the use of a Non-Uniform Rational B-Spline (NURBS) approximation on the parametric coordinate u. For that purpose, it will be necessary to calculate first the r-value anisotropic coefficient F at every 15° from the rolling direction and then use the NURBS approximation to build a function $F(u)$ that can generate the F-coefficient for any loading orientation θ. The Hill's 1948 [20] formulae for this coefficient can be used as presented in the following equation:

$$F(\theta) = \frac{H(1-4\sin^2\theta\cos^2\theta) - G(\sin^2\theta\cos^2\theta + r_\theta\cos^2\theta) + 2N\sin^2\theta\cos^2\theta}{\sin^2\theta\cos^2\theta + r_\theta\sin^2\theta} \tag{4}$$

This function for $F(\theta)$ is singular at 0° and so the following alternative function was used for the calculation of the coefficient at 0°:

$$F(0°) = \frac{2r_0}{r_{90}(1+r_0)} \tag{5}$$

For the NURBS approximation for both $C_a(u)$ and $F(u)$ the following relation between the angle from the rolling direction and the parametric coordinate u is necessary:

$$\theta = 2\pi u \tag{6}$$

and the angle θ can be easily obtained from the Mohr's circle or from the equation for the principal directions from plane stress analysis:

$$\tan(2\theta) = \frac{2\tau_{xy}}{\sigma_{xx} - \sigma_{yy}} \tag{7}$$

The coefficient $C_a(u)$ will be calculated from the new yield function from Eq. (2) and from the yield stresses σ_θ defined at every 15° from the rolling direction. From the stress transformation of the uniaxial loading to the anisotropic axes we can get:

$$\sigma_{xx} = \sigma_\theta \cos^2\theta$$
$$\sigma_{yy} = \sigma_\theta \sin^2\theta$$
$$\tau_{xy} = \sigma_\theta \cos\theta\sin\theta \tag{8}$$

and after replacing Eq. (8) into Eq. (2) the following is obtained for coefficient $C_a(u)$:

$$C_a(u) = \frac{\sigma_\theta}{\bar{\sigma}} \sqrt{\frac{3}{2}} \sqrt{\frac{(G+H)\cos^4\theta + [F(u)+H]\sin^4\theta + 2(N-H)\cos^2\theta\sin^2\theta}{F(u)+G+H}} \tag{9}$$

where $\frac{\sigma_\theta}{\bar{\sigma}}$ is the normalised flow stress at direction θ from the rolling direction obtained from experimental data.

2.1. Incorporation of the biaxial symmetric flow stress

The model defined so far does not consider the biaxial symmetric yield stress. If the stress tensor deviates considerably from the uniaxial stress state (defined by the principal stresses $\sigma_1 > 0$ and $\sigma_2 = 0$ for tension or $\sigma_2 < 0$ and $\sigma_1 = 0$ for compression), the differences in the accuracy can be substantial and this is more severe when the stress tensor is closer to the biaxial symmetric stress state. So, the incorporation of the biaxial symmetric flow stress in the model is important.

A generalised yield function in the normalised principal space, $\sigma_1/\bar{\sigma} - \sigma_2/\bar{\sigma}$ is shown in Fig. 1 and for each quadrant, the Mohr's circle with the possible loading directions is depicted. In the first quadrant ($\sigma_1 > 0$ and $\sigma_2 > 0$) it is possible to have a uniaxial tensile stress tensor defined with angle θ from the rolling direction, a biaxial tensile stress state and a biaxial symmetric tensile stress state, which is not represented by a circle but rather by a dot ($\sigma_1 = \sigma_2$). In the second and forth quadrant, the applied loading leads to a shear stress state ($\sigma_1 > 0$ and $\sigma_2 < 0$ or $\sigma_1 < 0$ and $\sigma_2 > 0$) and in the third quadrant it is possible to have a uniaxial compressive stress tensor defined with angle θ from the rolling direction, a biaxial compressive stress state and a biaxial symmetric compressive stress state.

The material calibration in most of well-known yield functions requires several mechanical tests: uniaxial tests for r-values and directional flow stresses and mechanical tests for the equi-biaxial stress (or bulge test) and the disk compression for the equi-biaxial r-value. The results from these tests are then included in optimisation algorithms for the calculation of the anisotropic coefficients, a procedure that is very common for example with the Barlat yield functions for aluminium [5,6]. The stress tensor as one transits from a symmetric biaxial state through an unsymmetric biaxial state to a uniaxial stress state remains unknown, however it is postulated in this work that a linear variation is valid. Hence an interpolation scheme is thus proposed between a uni-axial stress and a biaxial symmetric flow stress. The Mohr circle from Fig. 2 shows how far the stress state is from uniaxial stress conditions, or alternatively, how close it is to symmetric biaxial stress state. If $\sigma_2 = 0$ we have uniaxial stress state and if $\sigma_2 = \sigma_1$ we then have symmetric biaxial stress state. We can therefore interpolate between these two stress states by introducing a parameter β defined in Eqs. (11) and (12) that represents the deviation from a symmetric biaxial stress state.

Therefore, we can define a coefficient $C_b(u)$ for the biaxial symmetric stress state and the coefficient $C_a(u)$ becomes:
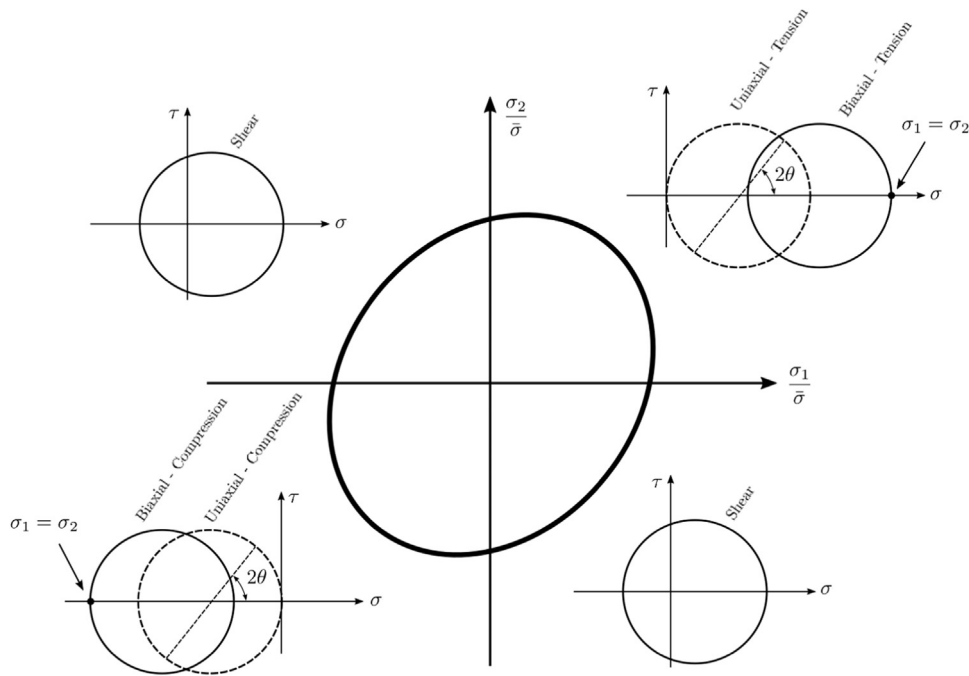
Fig. 1. Yield function and Mohr's circles at different quadrants representing different loading directions.
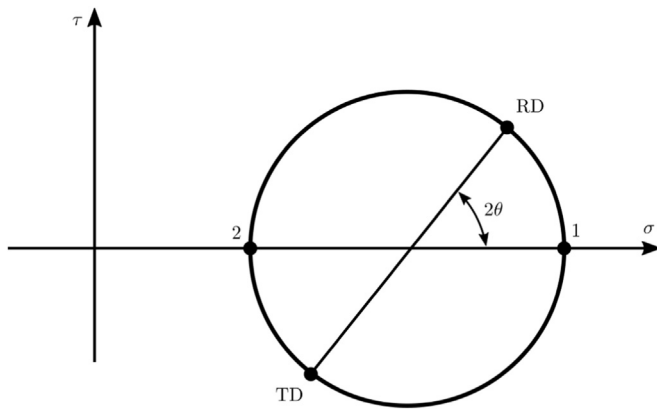

Fig. 2. Mohr's circle for a generalised biaxial stress state.

$$C(u, \beta) = \beta \cdot C_a(u) + (1 - \beta) \cdot C_b(u) \tag{10}$$

where:

$$\beta = \frac{\sigma_1 - \sigma_2}{\sigma_1} \tag{11}$$

for biaxial tension and:

$$\beta = \frac{|\sigma_2| - |\sigma_1|}{|\sigma_2|} \tag{12}$$

for biaxial compression. For $\beta = 0$ we have symmetric biaxial stress state and for $\beta = 1$ we have uniaxial stress. For $0 < \beta < 1$ we have a stress state somewhere between uniaxial and symmetric biaxial.

Thus, the new quadratic yield function from Eq. (2) becomes:

$$\bar{\sigma} = \frac{1}{C(u, \beta)} \sqrt{\frac{3}{2}} \sqrt{\frac{(G + H)\, \sigma_{xx}^2 + [F(u) + H]\, \sigma_{yy}^2 - 2H\sigma_{xx}\sigma_{yy} + 2N\tau_{xy}^2}{F(u) + G + H}}$$

$$\tag{13}$$

2.2. Iso-Shear contours for the yield locus

Another coefficient $C_c(u)$ can be introduced for greater flexibility of the yield locus for different (non-zero) iso-shear contour levels. This new coefficient can be added to the linear interpolation for the biaxial symmetric flow stress as described in Section 2.1. It is associated with the shear stress τ_{xy} in the following way:

$$\bar{\sigma} = \frac{1}{C(u, \beta) + C_c(u)\sqrt{\frac{\tau_{xy}}{\sigma_0}}} \sqrt{\frac{3}{2}} \times$$

$$\times \sqrt{\frac{(G + H)\, \sigma_{xx}^2 + [F(u) + H]\, \sigma_{yy}^2 - 2H\sigma_{xx}\sigma_{yy} + 2N\tau_{xy}^2}{F(u) + G + H}} \tag{14}$$

where σ_0 is the initial yield stress at 0^0 with the rolling direction. An example for the coefficient $C_c(u)$ for the Al2090 aluminium alloy used in the example of Section 5.1.2 is depicted in Fig. 3.
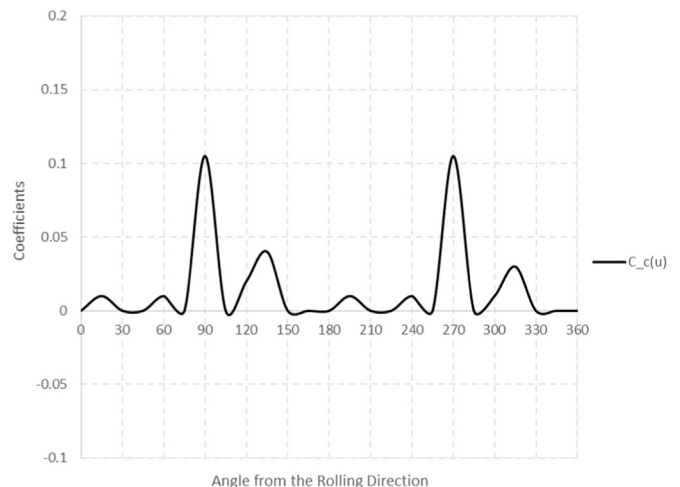

Fig. 3. Characterisation for the coefficient $C_c(u)$ for the Al2090 aluminium alloy.

3. Non-uniform rational B-spline (NURBS) for the representation of the non-constant coefficients

NURBS have been used extensively in geometric modelling because it is able to represent curves and/or surfaces with high complexity in their shape. Piegl [29], Hughes et al. [22] and Bazilevs et al. [7] addressed the most fundamental properties of the NURBS basis functions, however the most important attributes for this work are listed below:

1. They form a partition of unity, i.e.:

$$\sum_{J=1}^{m} N_J^p(u) = 1, \quad u \in U = [u_1, u_{m+p+1}];$$

(15)

2. The support of each $N_J^p(u)$ is compact and contained in $[u_I, u_{J+p+1}]$;
3. The basis functions are non-negative, that is, $\forall u \rightarrow N_J^p(u) \geq 0$;
4. Affine invariance.

3.1. Knot vector

An open knot vector is a set of non-negative parametric coordinates which are repeated $p + 1$ times at the beginning and at the end of the vector (p is the order of the polynomial basis functions). For one-dimensional basis functions of order p, the following generic open knot vector can be defined:

$$U = \{u_1, \ldots, u_{p+1}, \ldots, u_{m+1}, \ldots, u_{m+p+1}\}$$

(16)

where m is the number of control points or basis functions. The basis functions of order p have $p - 1$ continuous derivatives. More than one knot can be considered at the same parametric coordinate and it is thus referred as a repeated knot. An important property of repeated knots is that the continuous derivative of their basis functions is decreased by the number of times the knot is repeated. Also, the basis functions are interpolatory only if the knot's multiplicity is the same as the polynomial's order p [29]. For this quadratic yield function, the knot vector is defined for the limits $0.0 \leq u \leq 1.0$, where $u = 0.0$ corresponds to an angle $\theta = 0°$ with the rolling direction and $u = 1.0$ corresponds to an angle of $\theta = 360°$ with the rolling direction. For instance, for a quadratic degree in the NURBS basis functions ($p = 2$) we have the following knot vector:

$$U = \{0.0, 0.0, 0.0, 1.0, 1.0, 1.0\}$$

(17)

3.2. Basis functions, control points and approximation for the coefficients

For a specific local parametric coordinate u from an open knot vector and for a degree p of the polynomial, the basis functions are obtained recursively from the following formulae [13,22,29]:

$$N_I^p(u) = \frac{u - u_I}{u_{I+p} - u_I} N_I^{p-1}(u) + \frac{u_{I+p+1} - u}{u_{I+p+1} - u_{I+1}} N_{I+1}^{p-1}(u),$$

(18)

where I is the index for the basis functions. The formula for the basis functions in Eq. (18) must be initialised from piecewise basis functions corresponding to the polynomial order $p = 0$, i.e.:

$$N_I^0(u) = \begin{cases} 1 & if \quad u_I \leq u < u_{I+1} \\ 0 & otherwise \end{cases}$$

(19)

In this work, NURBS approximation functions are defined for the coefficients $C_a(u)$, $C_b(u)$ and $F(u)$ as follows:

$$\begin{aligned} F(u) &= \sum_I \frac{N_I(u) W_I F_I}{W} \\ C_a(u) &= \sum_I \frac{N_I(u) W_I C_{aI}}{W} \\ C_b(u) &= \sum_I \frac{N_I(u) W_I C_{bI}}{W} \end{aligned}$$

(20)

with:

$$W = \sum_I N_I(u) W_I$$

(21)

We will use the weights W_I equal to 1.0 and because of the partition of unity property of the NURBS basis functions ($\sum_I N_I(u) = 1$), the NURBS approximations are reduced to:

$$\begin{aligned} F(u) &= \sum_I N_I(u) F_I \\ C_a(u) &= \sum_I N_I(u) C_{aI} \\ C_b(u) &= \sum_I N_I(u) C_{bI} \end{aligned}$$

(22)

In Eq. (22), $N_I(u)$ are the NURBS basis functions which are used to approximate the coefficients $F(u)$, $C_a(u)$ and $C_b(u)$. F_I, C_{aI} and C_{bI} are the control points, whose definition can be found in the works of Piegl and Tiller [29]. A detailed description on how these control points are obtained for the current work can be found in Appendix B. The use of the same basis functions for all coefficients is the first advantage of the use of NURBS. Another important advantage of using NURBS is that they have local compact support, i.e. for a particular u in the parametric domain, only $p + 1$ control points in the domain of influence need to be used because outside of this domain of influence all other NURBS approximation functions are zero. In this work, $p = 2$ is used for the NURBS basis functions.

4. Return mapping procedure

From a phenomenological point of view, the plastic flow can be interpreted as an irreversible process in a material body, typically a metal, characterised in terms of the history of the strain tensor ϵ and two additional variables: the plastic strain ϵ^p and a suitable set of internal variables $\boldsymbol{\alpha}$ often referred to as hardening parameters. Conventional constitutive laws which represent plastic deformation of metals are typically described by considering three parts: yield functions, stress-strain (or hardening) functions and the associated normality flow rule. The yield function describes yield stresses in general deformation states, which are relative values measured with respect to a reference yield stress. The stress-strain function represents the work-hardening behaviour of the reference stress, which is usually a uniaxial or balanced biaxial tension stress.

The notion of irreversibility of plastic flow is expressed by the following equations of evolution for the set of internal variables $\{\epsilon^p, \boldsymbol{\alpha}\}$, called flow rule and hardening law, respectively:

$$\begin{aligned} \dot{\epsilon}^p &= \dot{\gamma} \mathbf{r}(\boldsymbol{\sigma}, \boldsymbol{\alpha}) \\ \dot{\boldsymbol{\alpha}} &= \dot{\gamma} \mathbf{H}(\boldsymbol{\sigma}, \boldsymbol{\alpha}) \end{aligned}$$

(23)

where $\mathbf{r}(\boldsymbol{\sigma}, \boldsymbol{\alpha})$ and $\mathbf{H}(\boldsymbol{\sigma}, \boldsymbol{\alpha})$ are prescribed functions which define the direction of plastic flow and the type of hardening. The parameter $\dot{\gamma}$ is a non-negative function, called the consistency parameter, which is assumed to obey the following Kuhn-Tucker complementary conditions:

$$\begin{aligned} \dot{\gamma} &\geq 0 \\ f(\boldsymbol{\sigma}, \boldsymbol{\alpha}) &\leq 0 \\ \dot{\gamma} f(\boldsymbol{\sigma}, \boldsymbol{\alpha}) &= 0 \end{aligned}$$

(24)

where $f(\boldsymbol{\sigma}, \boldsymbol{\alpha}) = \overline{\sigma} - \rho(\epsilon^p)$, with ρ being the stress value from the uniaxial stress-strain curve. In addition to the Kuhn-Tucker complementary conditions there are the consistency requirement, i.e.:

$$\gamma \dot{f}(\boldsymbol{\sigma}, \boldsymbol{\alpha}) = 0 \tag{25}$$

The consistency requirement allows the unloading to an elastic stress state ($\dot{f}(\boldsymbol{\sigma}, \boldsymbol{\alpha}) < 0$ and consequently $\gamma = 0$) and it also demonstrates that the stress tensor is always located at the yield surface ($\dot{f}(\boldsymbol{\sigma}, \boldsymbol{\alpha}) = 0$ and so $\gamma > 0$).

When using associated flow rule, the plastic strain tensor can be obtained directly from the yield potential as follows:

$$^{\Delta t}\boldsymbol{\epsilon}^p = \Delta\gamma \frac{\partial \overline{\sigma}}{\partial \boldsymbol{\sigma}} \tag{26}$$

When using the forward-Euler scheme for return mapping procedures [9,34,39,40], the time steps are assumed to be small enough for the coefficients $C_a(u)$ and $F(u)$ to be considered constant during return mapping. However, for larger time steps, the derivative of the equivalent yield stress obtained from the following chain rule can be used:

$$^{\Delta t}\boldsymbol{\epsilon}^p = \Delta\gamma \left(\frac{\partial \overline{\sigma}}{\partial \boldsymbol{\sigma}} + \frac{\partial \overline{\sigma}}{\partial C(u)} \frac{\partial C(u)}{\partial u} \frac{\partial u}{\partial \boldsymbol{\sigma}} + \frac{\partial \overline{\sigma}}{\partial F(u)} \frac{\partial F(u)}{\partial u} \frac{\partial u}{\partial \boldsymbol{\sigma}} \right) \tag{27}$$

where:

$$\frac{\partial C(u)}{\partial u} = \sum_I \frac{dN_I(u)}{du} C_I$$
$$\frac{\partial F(u)}{\partial u} = \sum_J \frac{dN_J(u)}{du} F_J \tag{28}$$

and $\partial u/\partial \boldsymbol{\sigma}$ is obtained from the derivative of Eqs. (6) and (7). If an associated flow rule is used and if the return mapping of the trial stress state to the yield surface is considered to be along the path with the closest distance to the yield function then the derivative $\partial u/\partial \boldsymbol{\sigma}$ can be assumed to be zero and so the plastic strain tensor from Eq. (27) reduces to:

$$^{\Delta t}\boldsymbol{\epsilon}^p = \Delta\gamma \frac{\partial \overline{\sigma}}{\partial \boldsymbol{\sigma}} \tag{29}$$

which simplifies considerably the return mapping procedure.

In the forward-Euler scheme for return mapping, the stress tensor can be corrected from the predictor stage as follows:

$$^{t+\Delta t}\boldsymbol{\sigma} = \boldsymbol{\sigma}^{trial} - \mathbf{D}^{\Delta t}\boldsymbol{\epsilon}^p = \boldsymbol{\sigma}^{trial} - \mathbf{D}\Delta\gamma \frac{\partial \overline{\sigma}}{\partial \boldsymbol{\sigma}} \tag{30}$$

The r-value is by definition obtained from the plastic strain in the width direction over the plastic strain along the thickness direction, i.e.:

$$r_\theta = \frac{\epsilon^p_{\theta+\pi/2}}{-(\epsilon^p_\theta + \epsilon^p_{\theta+\pi/2})} \tag{31}$$

and using Eq. (26) and the stress transformation Eq. (8), the following result for the r-value can be obtained:

$$r_\theta = \frac{H + [2N - F(u) - G - 4H]\sin^2\theta\cos^2\theta}{F(u)\sin^2\theta + G\cos^2\theta} \tag{32}$$

where it can clearly be seen that the r-value can be matched by adjusting the parameter $F(u)$ accordingly.

5. Validations and discussion

For validating the proposed quadratic yield function, single element uniaxial simulations are performed along every 15 degrees from the rolling direction for different case studies. The predicted r-values and flow stresses are compared with experimental results and with predictions from different yield criteria such as Hill's 1948, "yld91" (Barlat and Lian [3]), "yld96" (Barlat et al. [4]), "yld2000" (Barlat et al. [5]), "CPB06ex2" (Cazacu et al. [11]) and the new quadratic yield function, "YldParam", proposed in this paper.

Fig. 4 shows the procedure used for the prediction of r-values. As shown in Fig. 4, a $1 \times 1 \times 0.1$ mm single element is elongated and then

unloaded to eliminate the elastic deformation, since r-value is a plastic property. An additional boundary condition to impose equal vertical displacement was also considered for the nodes on the top of the element square.

The predicted r-value for an angle θ with the rolling direction is defined as:

$$r_\theta = -\frac{\epsilon_{22}}{\epsilon_{22} + \epsilon_{11}} \tag{33}$$

where:

$$\epsilon_{11} = \ln\left(1 + \frac{dx}{x}\right)$$
$$\epsilon_{22} = \ln\left(1 + \frac{dy}{y}\right) \tag{34}$$

This simple one-element test is going to be used with the different yield criteria listed above for the assessment of the accuracy of the different yield models for plastic anisotropy. These validations are going to be performed for three different alloys (case studies): two aluminium alloys AA6022 and AA2090, for weak and strong plastic anisotropy validations, and also for the AZ31B Mg alloy, where the main objective is to demonstrate the generality and accuracy of the new yield function in describing the plastic anisotropy as well as the asymmetry in tension-compression.

5.1. r-values and directional flow stresses for FCC materials

5.1.1. The AA6022 aluminium alloy

The Young's modulus and Poisson's ratio used were: $E = 70000.0$ MPa and $\nu = 0.3$, respectively. The following Voce's curve was used for strain hardening:

$$\overline{\sigma} = 328.36 - 194.5 \cdot \exp\left(-10.941 \cdot \overline{\epsilon}^p\right) \tag{35}$$

In Fig. 5, the yield locus projected on the zero shear stress plane, $\tau_{xy} = 0$, is shown for Hill's 1948, Barlat yld2000 and the new quadratic yield function (the stresses are normalised from the uniaxial stress at 0 degrees (σ_0)). It can be seen that the new yield function delivers a yield locus which is almost coincident with the yield locus from Barlat et al. [5], yld2000, but considerably different from the yield locus of Hill's 1948 yield criterion. It can be also seen that the symmetric biaxial yield stress was captured very well with this new yield function.

In Fig. 6, the yield locus contours for every 0.5 values of shear stress is shown, where the shape of the different yield locus is projected at different shear stress planes. Fig. 7 shows a plot of coefficients $F(u)$, G, H, N, $C_a(u)$ and $C_b(u)$ as a function of the angle with the rolling direction. The coefficients G, H and N are constants but the coefficients $F(u)$, $C_a(u)$ and $C_b(u)$ are not constant, they are function of the parametric variable u which in turn represents the angle measured from the rolling direction. The plots for the non-constant coefficients is symmetric about 180°, as expected for this alloy because there is no difference in its behaviour when in tension compared to when in compression. Another important aspect that is noteworthy from the plot of the coefficients in Fig. 7 is the comparison between $C_a(u)$ and $C_b(u)$. It can be seen that these two coefficients are the same at every orientation except at orientations in the vicinity of the symmetric biaxial stress region. This was also expected considering the coefficient $C_a(u)$ was designed to fit the uniaxial yield (flow) stresses, while the coefficient $C_b(u)$ was designed for the symmetric biaxial stress state.

Fig. 8 shows the prediction for the r-values and a comparison with experimental results. It can be seen that the new quadratic yield function predicts the r-values for every direction very well. Hill's 1948 shows a good agreement at 0°, 45° and 90° and the same can be said for the Barlat yield functions yld96 and yld2000. The prediction of r-values for the Barlat yield functions at every 15° from the rolling direction is not as good as the new yield function because the

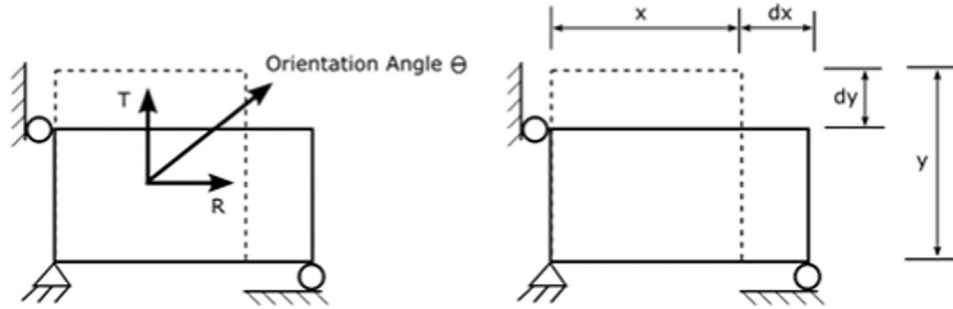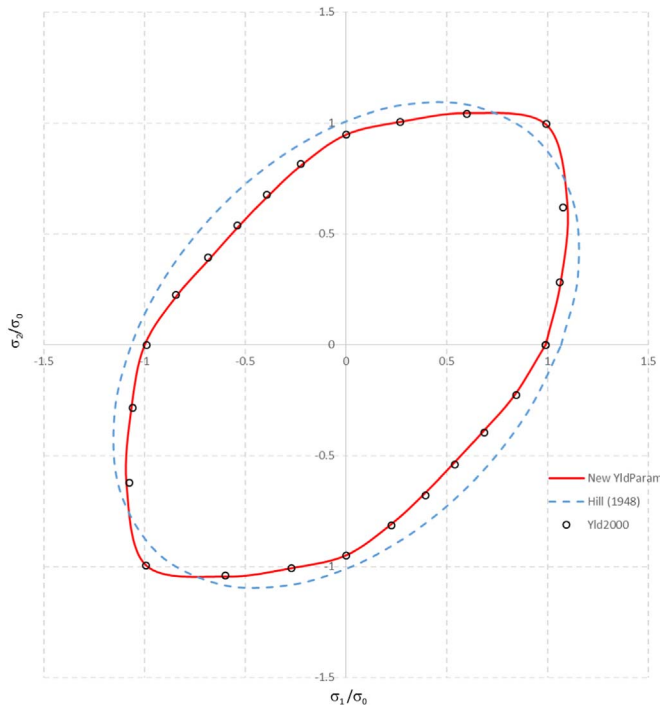**Fig. 4.** Definitions for r-value calculation.

Fig. 5. Yield locus for AA6022: comparison between Hill's 1948, yld2000 and the new yield function ($\tau_{xy} = 0$). Stresses normalised with the yield stress at 0 degrees (σ_0).

Fig. 6. Yield locus contours for AA6022 projected on shear planes for every 0.5 shear stress.

coefficients for Barlat yield functions were designed to fit r-values at 0°, 45° and 90° only and so we cannot expect a perfect prediction for all other directions. On the contrary, the coefficient $F(u)$ for the new yield function was designed to fit r-values at every direction and this explains the better accuracy of the newly proposed model.

In Fig. 9 the predictions for the normalised flow stresses at every 15° from the rolling direction are compared. Again, the comparison is made for the same yield models used for the r-values prediction and a comparison is also made with experimental results. The flow stresses for the new quadratic yield function were obtained following the derivation from Eq. (9), i.e.:

$$\frac{\sigma_\theta}{\bar{\sigma}} = C_a(u) \sqrt{\frac{2}{3}} \sqrt{\frac{F(u) + G + H}{(G + H)\cos^4\theta + [F(u) + H]\sin^4\theta + 2(N - H)\cos^2\theta\sin^2\theta}}$$

(36)

All yield criteria deliver normalised flow stresses very close to experimental results with the exception of Hill's 1948 yield criterion. It is also fair to say that the disparity for the Hill's results for the normalised yield stresses is expected because in this work the Hill coefficients were designed to fit the r-values and not the normalised flow stresses.

5.1.2. The Al2090 aluminium alloy

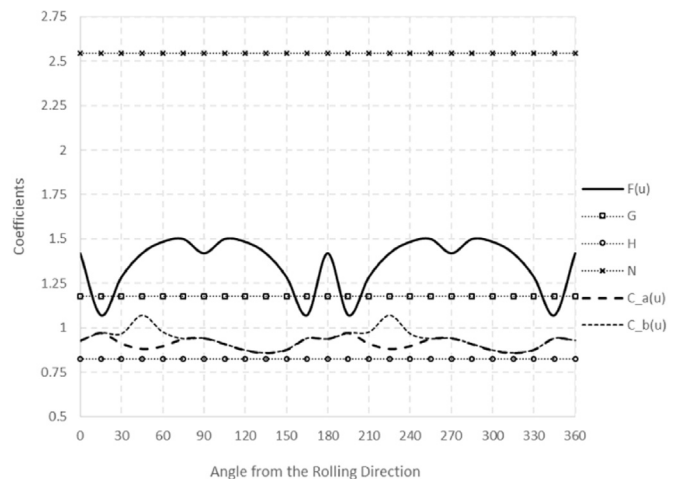The aluminium alloy AA6022 does not represent an alloy with a

Fig. 7. Coefficients $F(u)$, G, H, N, $C_a(u)$ and $C_b(u)$ for the AA6022 aluminium alloy.

strong plastic anisotropy. This can be clearly seen from Figs. 8 and 9 for the low amplitude for both the r-values and for the normalised flow stresses. The aluminium alloy AA2090, on the contrary, shows a very strong plastic anisotropy with high amplitudes or range for both r-
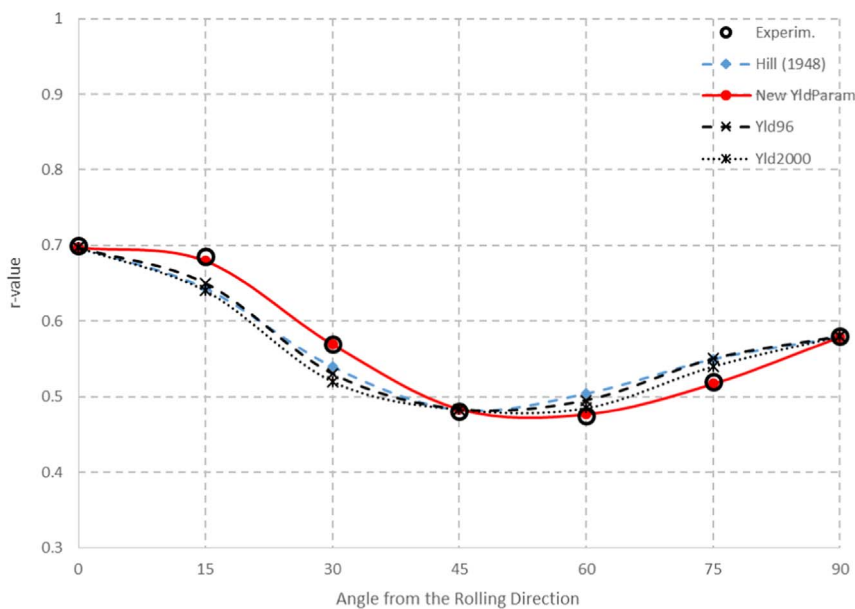
Fig. 8. Comparison between measured and predicted r-values for the AA6022 aluminium alloy.

values and normalised flow stresses and thus it represents a higher challenge for the newly proposed quadratic yield function.

The Young's modulus and Poisson's ratio used in this validation were: $E = 70000.0$ MPa and $\nu = 0.3$, respectively. The following Power law was used for strain hardening:

$$\bar{\sigma} = 646.0 \cdot (0.025 + \bar{\epsilon}^p)^{0.227} \tag{37}$$

In Fig. 10, the yield locus projected on the zero shear stress plane, $\tau_{xy} = 0$, for the Hill's 1948 and the new quadratic yield function is shown together with some experimental results. The stresses were normalised with the uniaxial stress at 0 degrees (σ_0). It can be seen that the new yield function delivers a yield locus which matches excellently well with the experimental results. It is quite interesting to see the difference in the yield locus when compared with the Hill's 1948 yield function; Hill's 1948 does not fit the biaxial symmetric flow stress accurately as expected because it does not have included the equi-biaxial stress in his model. On the contrary, the equi-biaxial yield stress was very well captured with this new quadratic yield function. Another noteworthy point is the ability of predicting the aluminium's behaviour

from the use of quadratic yield functions with an associated flow rule. It is well-agreed up till now that if an associated flow rule is used with aluminium alloys than the yield criterion needs to be non-quadratic, otherwise erroneous predictions for r-values and/or normalised yield stresses should be expected. Alternatively, if a non-associated flow rule is to be used, then a quadratic yield potential, such as Hill's 1948, should be able to accurately represent the aluminium's behaviour. The main reason is that with a non-associated flow rule the yield potential can be used to match the normalised yield stresses while the plastic potential can be used to match the r-values. Barlat yield functions (yld91, Barlat et al. [3], yld96, Barlat et al. [4] and yld2000, Barlat et al. [5]) were all designed to be non-quadratic yield functions as well as the CPB06ex2 yield function of Cazacu et al. [11].

In Fig. 11 the yield locus contours for every 0.5 values of shear stress is shown. In Fig. 12, a plot of the coefficients $F(u)$, G, H, N, $C_a(u)$ and $C_b(u)$ is shown as a function of the angle from the rolling direction. Again, the coefficients G, H and N are constant but the coefficients $F(u)$, $C_a(u)$ and $C_b(u)$ are not. The plots of these two non-constant coefficients show again a symmetry at $180°$. It is also worth noting for this example
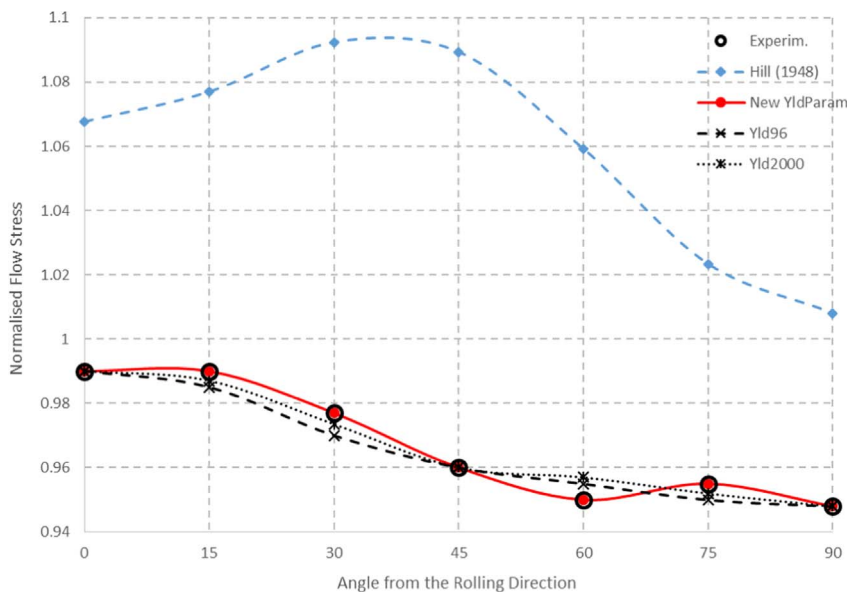

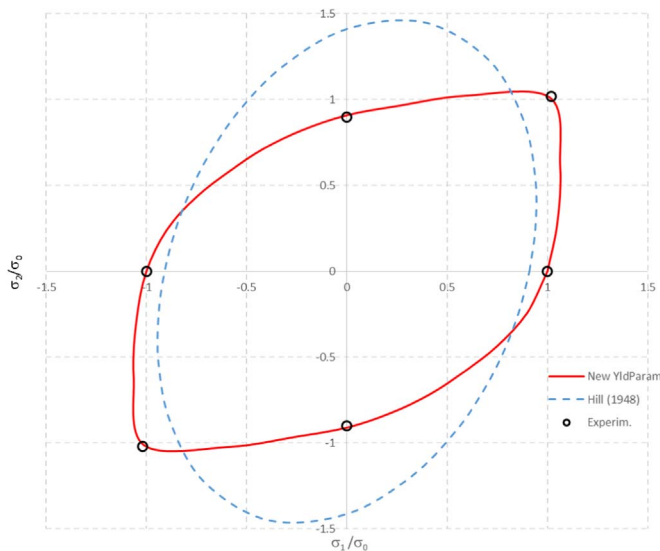Fig. 9. Comparison between measured and predicted flow stresses for the AA6022 aluminium alloy.

Fig. 10. Yield locus for Al2090: comparison between Hill 1948, the new parametric yield function and experimental results.
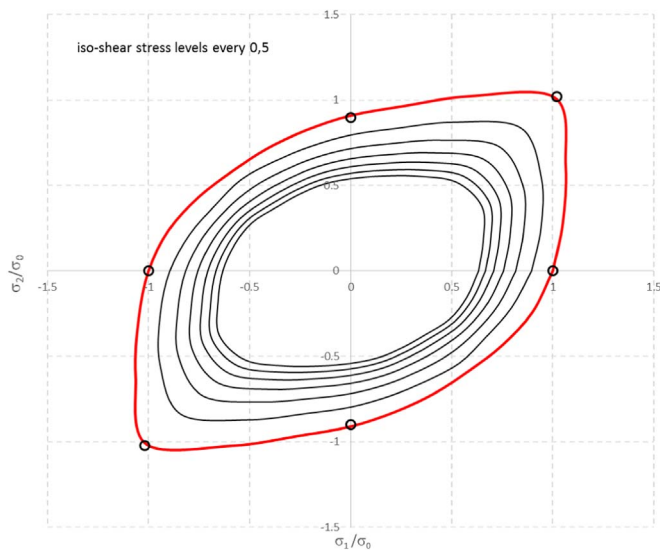

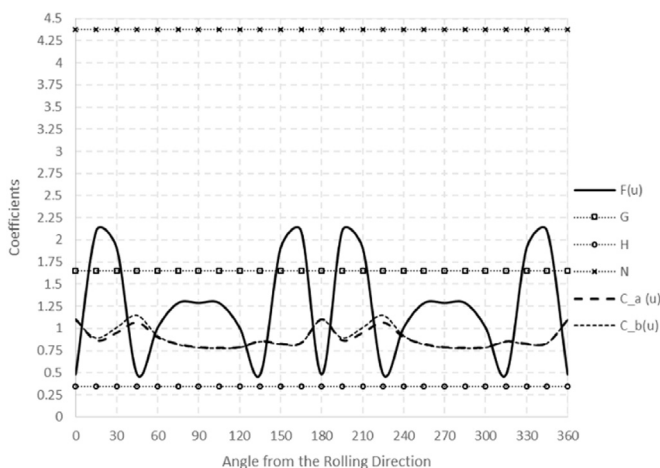**Fig. 11.** Yield locus contours for Al2090 projected on shear planes for every 0.5 shear stress.

Fig. 12. Coefficients $F(u)$, G, H, N, $C_a(u)$ and $C_b(u)$ for the Al2090 aluminium alloy.

the comparison between $C_a(u)$ and $C_b(u)$ as discussed in the previous section but, although, the deviation is not as prominent for this alloy because the effect of the symmetric biaxial stress is much less when compared to that of the AA6022 aluminium alloy.

Fig. 13 shows the comparison between the predicted r-values and experimental results. It can be seen that the predictions for the r-values from the new quadratic yield function match the experimental results for every orientation very well, with a slight deviation at 60°. Hill's 1948 gives good agreement at 0°, 45° and 90° and the same can be said for the Barlat yield functions yld91, yld96 and yld2000. The prediction of r-values for the Barlat yield functions at every 15° from the rolling direction is not as good as the new quadratic yield function because the coefficients for Barlat yield functions were designed to fit r-values at 0°, 45° and 90° only and so we cannot expect a perfect prediction for all other directions. On the contrary, the coefficient $F(u)$ for the new quadratic yield function was designed to fit r-values at every direction and this explains the better accuracy of the proposed model.

All yield criteria shown deliver normalised flow stresses very close to experiments with the exception of Hill's 1948 yield criterion as seen in Fig. 14. It can also be said that the Barlat yield criteria (yld91 and yld96) struggles a bit to match the experimental normalised flow stress at 30°. As discussed in the previous section, it is fair to say that the disparity for the Hill's results for the normalised yield stresses is expected because Hill coefficients in this work were designed to fit the r-values, not the normalised flow stresses. If the Hill coefficients had been fitted for the normalised yield stresses we should then expect a much better prediction of the Hill model for the normalised yield stresses but then the prediction for the r-values would be worst.

5.2. Cup drawing for earing prediction

The new yield function was also tested for a cup drawing simulation for the prediction of the cup earing profile for an Al 2090-T3 aluminium alloy.

Fig. 15 depicts the geometry for the die tools and for the blank sheet. The following dimensions were used in our analysis:

- Punch diameter: $D_p = 97.46$ mm
- Punch profile radius: $r_p = 12.70$ mm
- Die opening diameter: $D_d = 101.48$ mm
- Die profile radius: $r_d = 12.70$ mm
- Blank radius: $D_b = 158.76$ mm

The material properties used in the analysis are given below:

- Stress-strain curve characteristics: $\overline{\sigma} = 646(0.025 + \overline{\epsilon})^{0.227}(MPa)$
- Initial sheet thickness: $t_0 = 1.6$ mm
- Coulomb coefficient of friction: 0.1
- Blank holding force: 22.2 kN

The cup drawing simulation was carried out in the commercial software ABAQUS and by using a user material subroutine "VUMAT" for the new yield function. Fig. 16 depicts the deformed configuration and the earing profile for the cup after the cup drawing operation.

In Fig. 17 the cup earing profile is compared for the experimental results from Yoon et al. [41], Yld96 without translation [41] (or without consideration of the strength differential effects) and the new yield function. For an orthotropic material, the cup height profile between 0 and 90 degrees should be the mirror image of the cup height profile between 90 and 180 degrees with respect to the 90 degrees axis. However, the measured earing profile slightly deviates from this condition and, according to Yoon et al. [41], this deviation might have occurred because the center of the blank was not aligned properly with the centers of the die and the punch during processing. The earing magnitude is in good agreement with the simulations of Yoon et al. [41] for the Yld96 without translation and also in reasonable agreement with
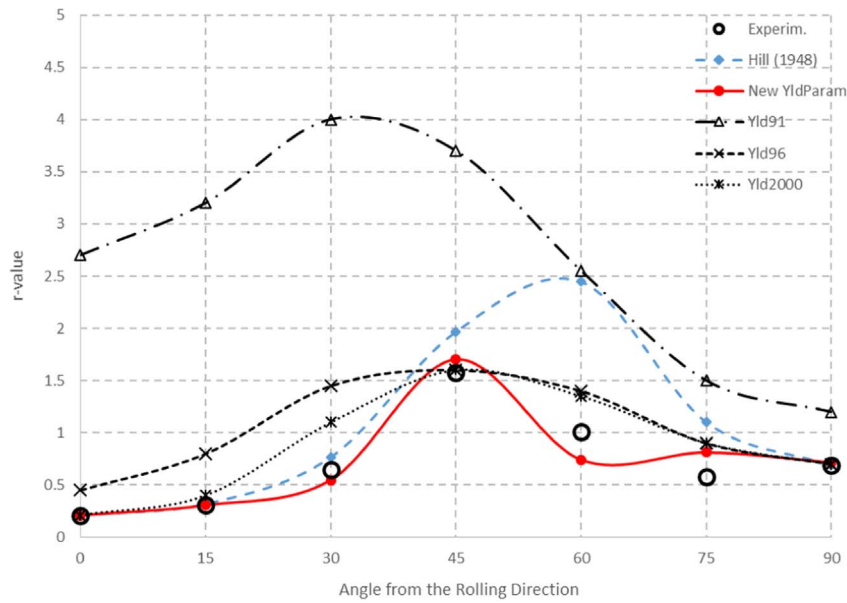
Fig. 13. Predictions and experimental results for the r-values of the Al2090 aluminium alloy.

the measured result, but however, both Yld96 and the new yield function do not lead to the correct trend: the experimental cup height at 0 degrees is larger than that at 90 degrees, whereas the simulated results predict the reverse. Yoon et al. [41] and Yoon et al. [43] reported this to be a consequence of the cup drawing simulations being performed from coefficients based on the tensile test results. In their work, Yoon et al. [41] said that since the stresses in the flange area are nearly compressive in nature, the cup drawing simulations should also account for the compressive test results. In other words, they are suggesting that there is a strength differential effect that should have been considered during the material characterisation of the Al2090 aluminium alloy. It was shown in Yoon et al. [41] that if the strength differential effect was considered (Yld96 with translation of the yield surface) then a better agreement could be obtained with the experimental results. It is therefore more important to compare the results obtained with the new yield function with the results from the use of Yld96 without translation of the yield surface (both plotted in Fig. 17)
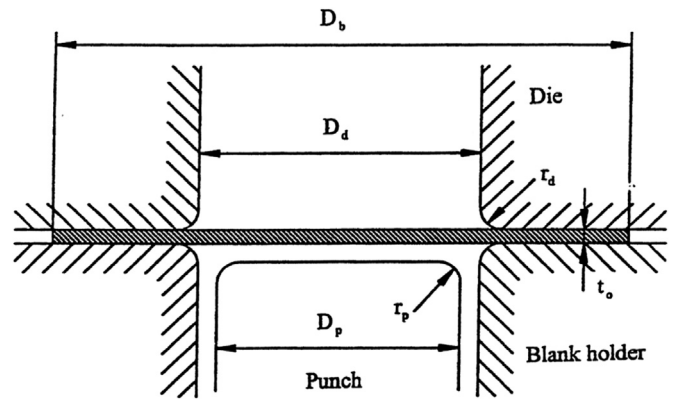

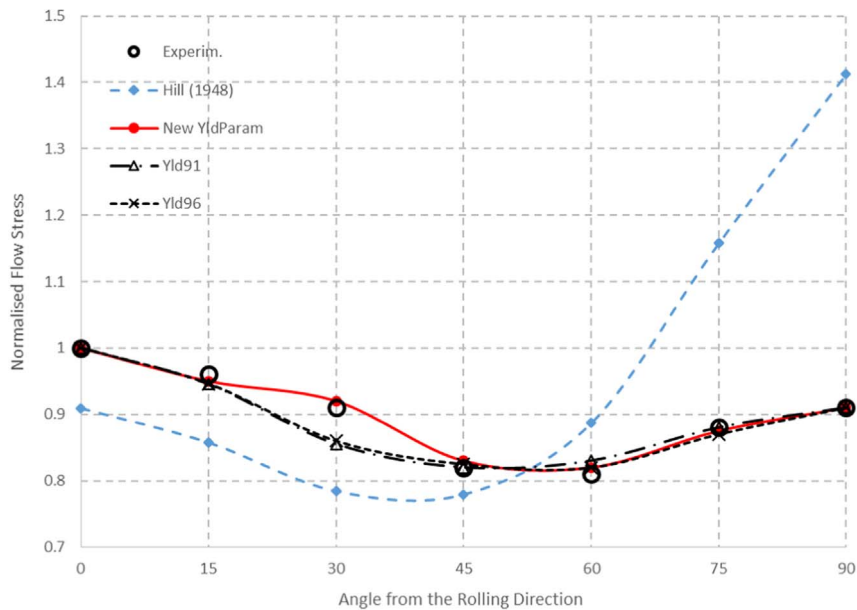**Fig. 15.** Al2090 cup forming example. Definition of tools and blank geometry.

Fig. 14. Comparison for predictions of flow stresses for the Al2090 aluminium alloy.
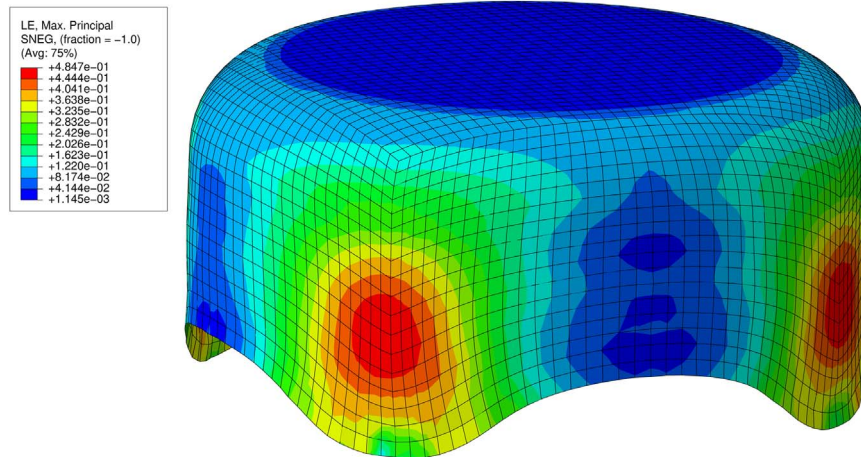
Fig. 16. Al2090 deformed cup after drawing.

as they properly reflect the material characterisation employed in the simulation.

For the Al2090-T3 alloy, Yoon et al. [42] demonstrated that a more accurate prediction of the r-value at 75 degrees should be reflected into a small ear around 15 degrees and so the earing profile should include six ears instead of four ears. This behaviour was not observed with the current model maybe due to the slight deviation of the r-value prediction obtained for 75 degrees from the rolling direction.

5.3. Iso-error maps

In this section we assess the accuracy of the return mapping procedure used in this work by means of the iso-error maps, as detailed in Simo and Hughes [34]. The new yield function developed in this work was designed to work with the semi-implicit or forward-Euler return mapping scheme, as detailed in Section 4 and as derived in a previous work of Cardoso and Yoon [9], where it is assumed that the trial stress state is not too far away from the yield locus or, in other words, the incremental time steps are considered to be sufficiently small enough. The iso-error maps presented in this section were constructed for the Al2090 alloy, whose yield locus has the shape as described in Fig. 10, including regions with high curvature, making the accuracy and even the convergence of the return mapping scheme much more complicated.

Three points on the yield surface were considered for the plotting of the iso-error maps: point A, corresponding to the uniaxial stress state; point B, which is a biaxial stress state; point C, which corresponds to the pure shear stress state. All of these points are schematically represented in Fig. 18.

Without any loss of generality, the initial stress state for points A, B and C is the one corresponding to locations at the yield locus for the initial yield point. Subsequently, incremental stresses in the principal directions "S1" and "S2" are added and the return mapping scheme is applied for the assessment of the iso-error contours. There is the need to calculate the exact stress tensor for points A, B and C after return mapping and that is done in this current work by applying 10,000 infinitesimal stress increments between the yield locus and the yield locus for the trial stress state. The iso-error contour E is constructed from the following equation:

$$E = \frac{\sqrt{(\boldsymbol{\sigma} - \boldsymbol{\sigma}^*) : (\boldsymbol{\sigma} - \boldsymbol{\sigma}^*)}}{\sqrt{\boldsymbol{\sigma}^* : \boldsymbol{\sigma}^*}} \times 100 \tag{38}$$

where $\boldsymbol{\sigma}^*$ is the exact stress tensor and $\boldsymbol{\sigma}$ is the stress tensor after return mapping.

The plots for the iso-error contours for points A, B and C in Figs. 19, 20 and 21, respectively, were constructed for $S1/Sy \leq 1.75$ and $S2/Sy \leq 1.75$, where Sy is the initial yield stress of Al2090 alloy. Because the return mapping scheme used in this work is a forward-Euler scheme
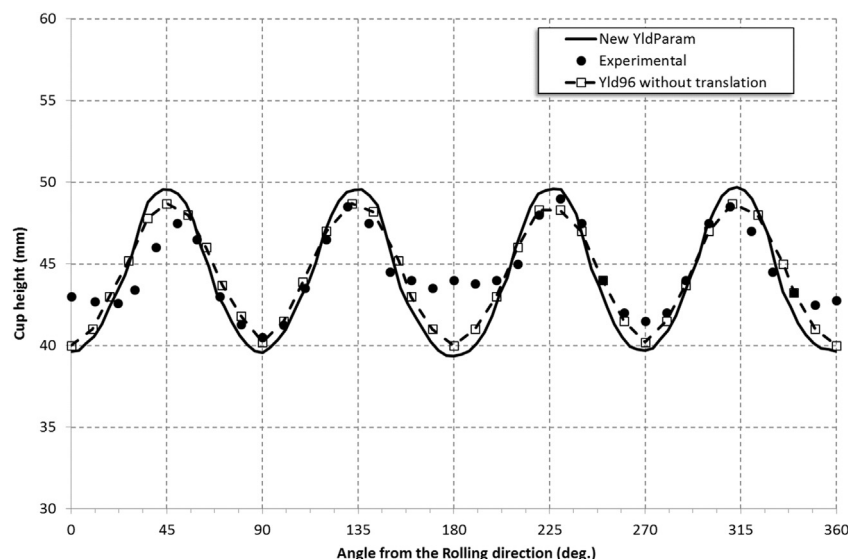

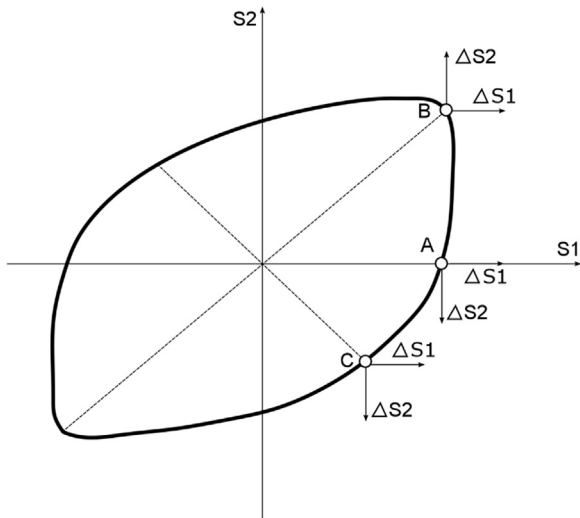**Fig. 17.** Cup earing profile for the Al2090 aluminium alloy.

Fig. 18. Points A (uniaxial), B (biaxial) and C (pure shear) for the iso-error maps.
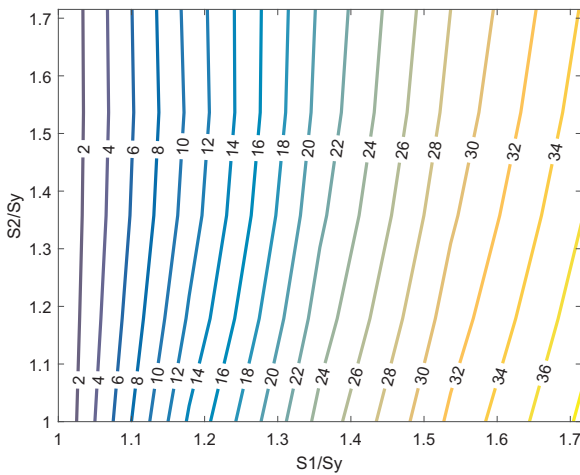

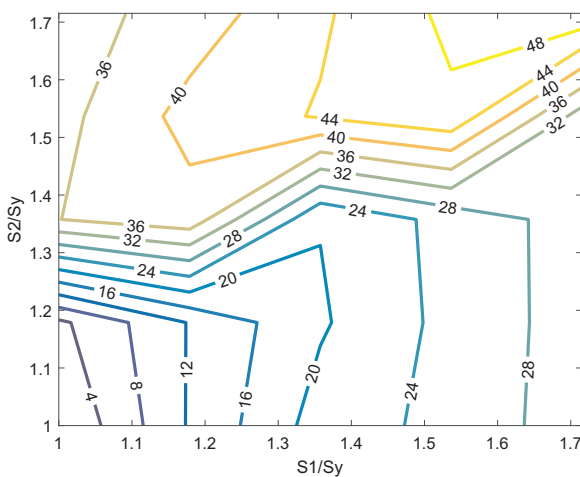**Fig. 19.** Iso-error plot for point A (uniaxial stress state).

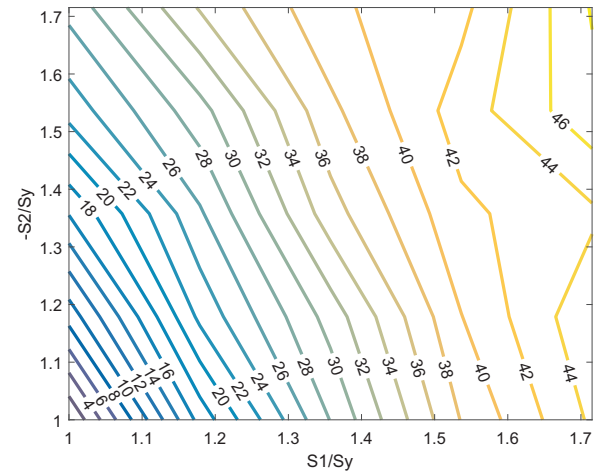**Fig. 20.** Iso-error plot for point B (biaxial stress state).

Fig. 21. Iso-error plot for point C (pure shear stress state).

for the forward-Euler scheme in the work of Cardoso and Yoon [9].

Another aspect that is worth discussing is the computational performance of the return mapping scheme used. This was addressed by Cardoso and Yoon [9], however the return mapping scheme now comes together with a new yield function so it is worth considering the computational costs or benefits added by the new yield function to the return mapping procedure. When compared with the yld96 function used for the cup drawing for the earing profile of previous section, it can be said that there is the need to calculate the loading direction as in Eq. (7), however this is computationally inexpensive. The other major difference of this new yield function is the calculation of the plastic flow direction, where in this case we calculate the normal to the yield surface (derivative of the yield potential) by using B-Splines basis functions and the derivative of the B-Spline's basis functions for the anisotropic coefficients. When comparing with the yld96 yield function, the normal to the yield surface also has to be calculated and the derivatives of the yield potential, however, for the approximation of the coefficients for a particular loading direction, only the coefficients inside the local compact support of the B-Spline basis functions need to be considered. If the polynomials used for the B-Splines basis function have degree "p" then the size of the local compact support is $p + 1$, so for a quadratic degree only three coefficients in the local compact support of the loading direction "u" need to be used. If we compare with more elaborated yield functions such as Barlat's yld2000, there are the advantages of the straightforwardness of obtaining the anisotropic coefficients as well as the simplicity for the calculation of the plastic flow tensor for the normal to the yield surface. In the comparison study carried out for the Al2090 alloy, the differences for the computational performance of the return mapping scheme used for the new yield function and for the yld96 and yld2000 yield functions are barely undetectable.

5.4. r-values and directional flow stresses for HCP materials

5.4.1. The AZ31B Mg alloy

The last case study presented in this paper is for a HCP material, the AZ31B Mg alloy. Many yield functions were developed to account for the asymmetry in tension-compression for these alloys and amongst them we can distinguish the works of Cazacu et al. [10,11] and more recently the work of Soare and Benzerga [35] on the modelling of asymmetric yield functions. The main objective of this case study is to demonstrate that the newly proposed yield function for plane stress analysis is generalised enough to accurately predict the plastic aniso-tropy for this alloy as well as its asymmetric behaviour in tension-compression. The Young's modulus and Poisson's ratio used were: $E = 42000.0$ MPa and $\nu = 0.35$, respectively. The following Voce curve

(traditionally used for explicit analysis), then if larger time steps (or larger $S1/Sy$ ratio) are used there is the chance of divergence in the return mapping scheme and that is even more critical for the high curvature yield locus of the Al2090 aluminium alloy. This was also proved to be the case when the Barlat yld2000 yield function was used
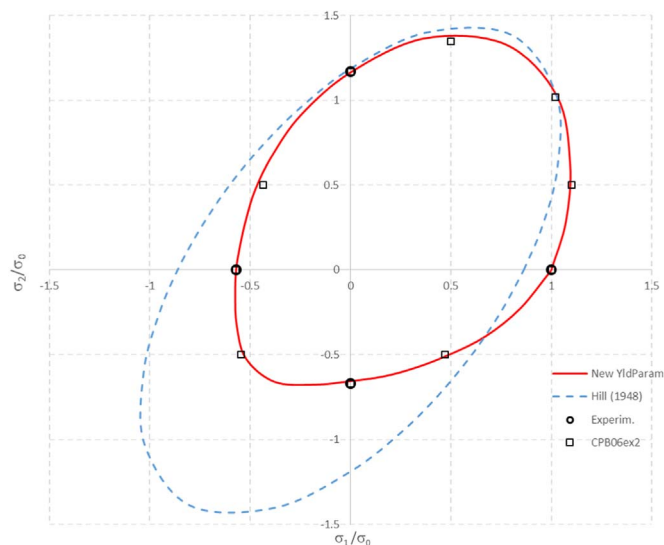
Fig. 22. Yield locus for AZ31B Mg alloy: comparison between Hill 1948, Plunkett et al. [31] for the CPB06ex2 yield function, the new parametric yield function and experiments from Lou et al. [27].

was used for strain hardening:

$$\bar{\sigma} = 361.43 - 158.6 \cdot \exp\left(-9.74 \cdot \bar{\epsilon}^p\right) \tag{39}$$

In Fig. 22, the yield locus for the Hill 1948 yield function, for Cazacu et al. [11] CPB06ex2 yield potential, for the newly proposed quadratic yield criterion (YldParam) and for the experimental results from Lou et al. [27] are presented. It can be seen that the proposed new yield function is able to predict accurately the asymmetry in tension-compression that is very typical of this alloy. The CPB06ex2 yield criterion is also extremely accurate but, as reported by Plunkett et al. [31], it requires the calculation of 18 anisotropic coefficients plus 2 additional coefficients to describe the asymmetry in tension-compression, it is not a quadratic yield potential and it requires at least two linear transformations for the yield potential. In Fig. 23 it is shown the yield locus contours for every 0.5 values of shear stress. It shows the shape of the different yield locus when projected at different shear stress planes.
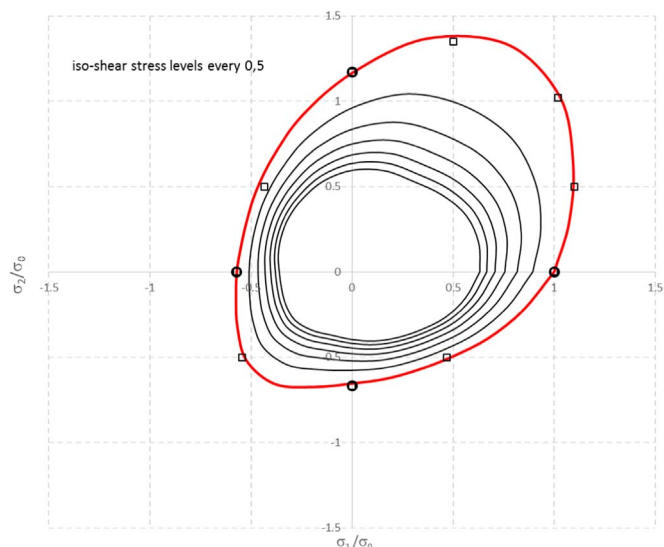

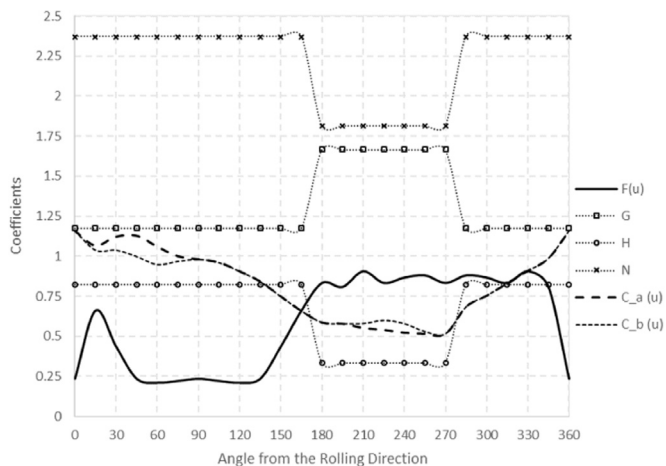**Fig. 23.** Yield locus contours for the AZ31B Mg alloy projected on shear planes for every 0.5 shear stress.

Fig. 24. Coefficients $F(u)$, G, H, N and $C_a(u)$ for the AZ31B Mg alloy.

Fig. 24 shows a plot of coefficients $F(u)$, G, H, N, $C_a(u)$ and $C_b(u)$ as a function of the angle from the rolling direction. It is important to notice that for this case study the coefficients G, H and N have different values for tension and compression and so are not constant for the entire range of loading directions. The reason for the different distribution for these coefficients is due to the asymmetric behaviour of HCP alloys, which requires a separated calibration for the tension and compression domains. The plot for the coefficients $F(u)$, $C_a(u)$ and $C_b(u)$ is not symmetric at $180°$ due to the asymmetric behaviour in tension-compression of this particular Mg alloy. Also, regarding the coefficients $C_a(u)$ and $C_b(u)$ from Fig. 24, and in particular their comparison in the vicinity of the symmetric biaxial stress state, it can be said that the difference between the coefficients is higher in tension than it is in compression.

Fig. 25 shows the r-values predictions and comparisons with experimental results for both the tension and compression regions. The prediction from the new yield function is compared with Plunkett et al. [31] predictions based on the yield criterion CPB06ex2 of Cazacu et al. [11]. It can be seen that the CPB06ex2 yield criterion is just perfect in accurately predicting the r-values for both tension and compression regions. The new yield function is also great for the prediction of the r-values in tension and some slight deviations are seen for the r-values in compression, mostly for $45°$ and $75°$. However, it is reasonable to say that these minor deviations are still good if we consider the fact that these predictions were obtained from the use of a quadratic yield potential. In regards to the normalised yield stresses from the plots in Fig. 26, the conclusion is that both Cazacu et al. [11] CPB06ex2 yield potential and the newly proposed formulation deliver excellent agreement with the normalised yield stresses from experiments.

In this paper, the general definition or classification of a "quadratic planar anisotropic yield function" is adopted. This commonly refers to the exponent used directly in the stress components inside the yield criterion, which in the case of this new yield function is of degree two as in the original Hill's yield criterion [20]. All non-quadratic (higher-order) yield functions in the literature are defined as such because of the higher exponent of the stress components and this invariably results in the more accurate fitting of the yield surface. This higher-order fitting however comes at such costs as difficulties in converging during return mapping procedures and also higher number of coefficients that must be obtained experimentally, amongst other costs. However, in this new function the same accurate fitting is achievable through the introduction of the variable anisotropic parameters C and F which are both functions of the angle between rolling and loading directions, which is one of the main advantages of this yield function. The curves
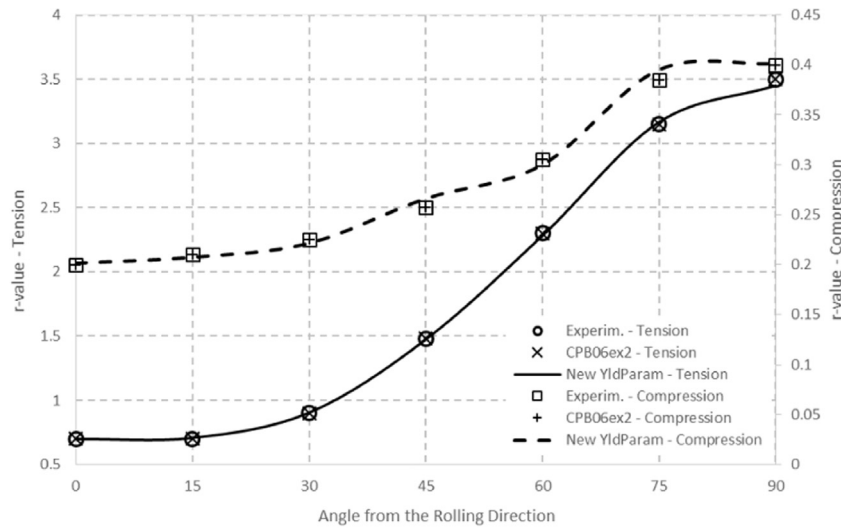
Fig. 25. Comparison between the predicted r-values (Tension and Compression) for the new yield function, Plunkett et al. [31] and experimental results for the AZ31B Mg alloy.
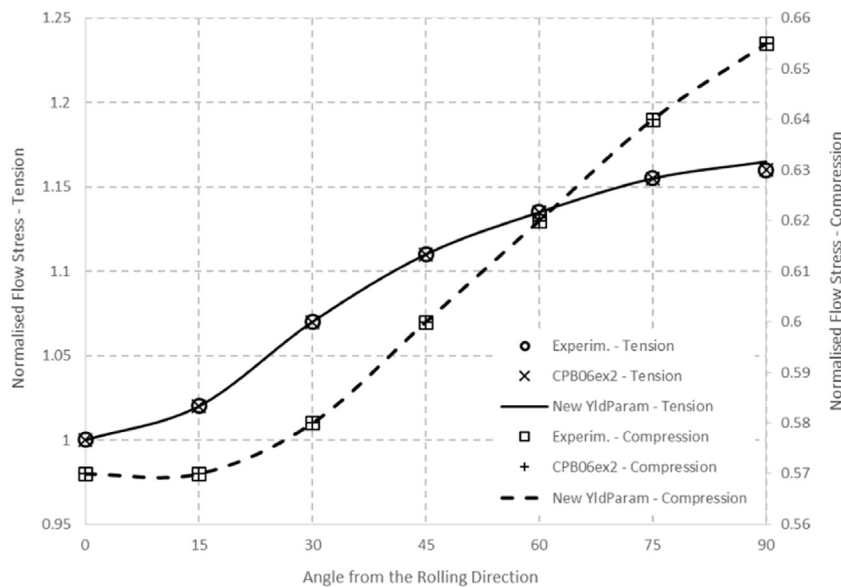

Fig. 26. Comparison between the predicted Normalised Flow Stress in Tension and Compression for the new yield function, Plunkett et al. [31] and experimental values for the AZ31B Mg alloy.

for the distribution of these anisotropic parameters are defined as a B-Spline function of the local parametric variable, however they can also be represented by any other function with any degree as far as an accurate fitting of the coefficient is achieved.

6. Concluding remarks

In this work, a new generalised quadratic yield function was developed for the description of planar plastic anisotropy in metallic alloys. The new yield function delivers a good prediction of both r-values and directional flow stresses and it also accurately describes the biaxial symmetric flow stress and the unsymmetric biaxial stress state. One coefficient $F(u)$ was made function of a directional parameter that represents the angle between the loading direction and the rolling direction. An additional coefficient $C(u)$ was added for the accurate

prediction of directional flow stresses. Quadratic NURBS basis functions were used for the mathematical description of these two coefficients, making the method computationally effective.

It was shown in the discussion/validations section that the yield locus, r-values and directional flow stresses predictions were almost perfectly matched for two aluminium alloys (AA6022 and AA2090), with weak and strong plastic planar anisotropy, and also for a HCP magnesium alloy (AZ31B Mg), where the asymmetric behaviour in tension-compression was also shown to be very well captured. In addition, FE simulations of the cup drawing of a circular blank was conducted, where the predicted earing profile matches the experimental results satisfactorily. These prove that the newly developed yield potential is generalised enough for the prediction of plastic planar anisotropy and for the accurate description of the asymmetry in tension-compression of HCP materials.

Appendix A. Proof of convexity in the principal stress space ($\tau_{xy} = 0$) and for the case of proportional loading

A yield function is convex if its Hessian matrix **H** defined as:

$$\mathbf{H} = \frac{\partial^2 \overline{\sigma}}{\partial \sigma_i \partial \sigma_j} \tag{A.1}$$

is positive semi-definite, i.e. if its eigenvalues are not negative (Rockafellar [33]). The analysis is going to be done initially for the yield function projected on the zero shear stress plane, i.e. for $\tau_{xy} = 0$. In this case the Hessian matrix is defined as follows:

$$\mathbf{H} = \begin{bmatrix} \frac{\partial^2 \overline{\sigma}}{\partial \sigma_{xx}^2} & \frac{\partial^2 \overline{\sigma}}{\partial \sigma_{yy} \partial \sigma_{xx}} \\ \frac{\partial^2 \overline{\sigma}}{\partial \sigma_{xx} \partial \sigma_{yy}} & \frac{\partial^2 \overline{\sigma}}{\partial \sigma_{yy}^2} \end{bmatrix} \tag{A.2}$$

The first derivatives are defined as:

$$\frac{\partial \overline{\sigma}}{\partial \sigma_{xx}} = A \frac{(G + H)\, \sigma_{xx} - H\sigma_{yy}}{\sqrt{(G + H)\, \sigma_{xx}^2 + [F(u) + H]\, \sigma_{yy}^2 - 2H\sigma_{xx}\sigma_{yy}}}$$

$$\frac{\partial \overline{\sigma}}{\partial \sigma_{yy}} = A \frac{(F(u) + H)\, \sigma_{yy} - H\sigma_{xx}}{\sqrt{(G + H)\, \sigma_{xx}^2 + [F(u) + H]\, \sigma_{yy}^2 - 2H\sigma_{xx}\sigma_{yy}}} \tag{A.3}$$

where:

$$A = \frac{1}{C(u)} \sqrt{\frac{3}{2(F(u) + G + H)}} \tag{A.4}$$

The second derivatives can be obtained from the following equations:

$$\frac{\partial^2 \overline{\sigma}}{\partial \sigma_{xx}^2} = \frac{A\, [G \cdot F(u) + G \cdot H + H \cdot F(u)]\, \sigma_{yy}^2}{\{(G + H)\, \sigma_{xx}^2 + [F(u) + H]\, \sigma_{yy}^2 - 2H\sigma_{xx}\sigma_{yy}\}^{3/2}}$$

$$\frac{\partial^2 \overline{\sigma}}{\partial \sigma_{xx} \partial \sigma_{yy}} = - \frac{A\, [G \cdot F(u) + G \cdot H + H \cdot F(u)]\, \sigma_{yy}\sigma_{xx}}{\{(G + H)\, \sigma_{xx}^2 + [F(u) + H]\, \sigma_{yy}^2 - 2H\sigma_{xx}\sigma_{yy}\}^{3/2}}$$

$$\frac{\partial^2 \overline{\sigma}}{\partial \sigma_{yy}^2} = \frac{A[G \cdot F(u) + G \cdot H + H \cdot F(u)]\, \sigma_{yy}^2}{\{(G + H)\, \sigma_{xx}^2 + [F(u) + H]\, \sigma_{xx}^2 - 2H\sigma_{xx}\sigma_{yy}\}^{3/2}} \tag{A.5}$$

and so the Hessian matrix can be written as:

$$\mathbf{H} = \frac{A[G \cdot F(u) + G \cdot H + H \cdot F(u)]}{\{(G + H)\, \sigma_{xx}^2 + [F(u) + H]\, \sigma_{yy}^2 - 2H\sigma_{xx}\sigma_{yy}\}^{3/2}} \begin{bmatrix} \sigma_{yy}^2 & -\sigma_{xx}\sigma_{yy} \\ -\sigma_{xx}\sigma_{yy} & \sigma_{xx}^2 \end{bmatrix} \tag{A.6}$$

The eigenvalues for this Hessian matrix are:

$$\alpha_1 = 0$$

$$\alpha_2 = \frac{A[G \cdot F(u) + G \cdot H + H \cdot F(u)]}{\{(G + H)\, \sigma_{xx}^2 + [F(u) + H]\, \sigma_{yy}^2 - 2H\sigma_{xx}\sigma_{yy}\}^{3/2}} (\sigma_{xx}^2 + \sigma_{yy}^2) \tag{A.7}$$

which means that the new yield function is convex if:

$$\frac{A\, [G \cdot F(u) + G \cdot H + H \cdot F(u)]}{\{(G + H)\, \sigma_{xx}^2 + [F(u) + H]\sigma_{yy}^2 - 2H\sigma_{xx}\sigma_{yy}\}^{3/2}} \geq 0 \tag{A.8}$$

or:

$$A[G \cdot F(u) + G \cdot H + H \cdot F(u)] \geq 0 \tag{A.9}$$

From Eq. (A.9), $A \geq 0$ means the coefficient $C(u)$ needs to be positive and the coefficients $F(u)$, G and H also need to be positive.

Appendix B. Control points for coefficients $C(u)$ and $F(u)$

The NURBS control points for the coefficients $C(u)$ and $F(u)$ were generated from the algorithm described in the work by Piegl and Tiller [29] where the major equations used are described here.

Given a set of points $\mathbf{F}_k (k = 0, \ldots, n)$, the aim is to interpolate these points with a second-degree nonrational B-spline curve. From the parameter $0 \leq u \leq 1$ that represents the angle between the loading and rolling directions, we can define a parameter $\overline{u}_k$ for each $\mathbf{F}_k$ and select an appropriate knot vector $U = \{u_0, \ldots, u_m\}$ so that the following $(n + 1) \times (n + 1)$ system of linear equations can be defined:

$$\mathbf{F}_k = \sum_{l=0}^{n} N_{l,2}(\overline{u}_k)\, \mathbf{P}_l \tag{B.1}$$

where $N_{i,2}(\overline{u}_k)$ stands for the quadratic NURBS basis function of control point $\mathbf{P}_l$, evaluated at the parametric coordinate $\overline{u}_k$. The control points $\mathbf{P}_l$ are the $n + 1$ unknowns in the linear system of equations. There are different methods for the definition of the parametric coordinates $\overline{u}_k$. In this work, we first defined the total chord length d as follows:

$$d = \sum_{k=1}^{n} |\mathbf{F}_k - \mathbf{F}_{k-1}| \tag{B.2}$$

and then the parametric coordinates were defined as:

$$\bar{u}_0 = 0$$
$$\bar{u}_n = 1$$
$$\bar{u}_k = \bar{u}_{k-1} + \frac{|\mathbf{F}_k - \mathbf{F}_{k-1}|}{d} \quad k = 1, \ldots, n - 1 \tag{B.3}$$

For more details on these, refer to the work by Piegl and Tiller [29].

References

[1] Balogh L, Capolungo L, Tome CN. On the measure of dislocation densities from diffraction line profiles: A comparison with discrete dislocation methods. Acta Mater 2012;60:1467–77.

[2] Barlat F, Lian J. Plastic behaviour and stretchability of sheet metals. Part I: A yield function for orthotropic sheets under plane stress conditions. Int J Plast 1989;5:51–66.

[3] Barlat F, Lege DJ, Brem JC. A six-component yield function for anisotropic materials. Int J Plast 1991;7:693–712.

[4] Barlat F, Maeda Y, Chung K, Yanagawa M, Brem JC, Hayashida Y, et al. Yield function development for aluminium alloy sheets. J Mech Phys Solids 1997;45:1727–63.

[5] Barlat F, Brem JC, Yoon JW, Chung K, Dick RE, Lege DJ, et al. Plane stress yield function for aluminium alloy sheets-part 1: theory. Int J Plast 2003;19:1297–319.

[6] Barlat F, Aretz H, Yoon JW, Karabin ME, Brem JC, Dick RE. Linear transformation based anisotropic yield functions. Int J Plast 2005;21:1009–39.

[7] Bazilevs Y, Calo VM, Cottrell JA, Evans JA, Hughes TJR, Lipton S, et al. Isogeometric analysis using T-Splines. Comput Methods Appl Mech Eng 2010;199:229–63.

[8] Bron F, Besson J. A yield function for anisotropic materials. Appl Alum Alloy Int J Plast 2004;20:937–63.

[9] Cardoso Rui PR, Yoon Jeong Whan. Stress integration method for a nonlinear kinematic/isotropic hardening model and its characterization based on polycrystal plasticity. Int J Plast 2009;25:1684–710.

[10] Cazacu O, Barlat F. Generalization of Drucker's yield criterion to orthotropy. Math Mech Solids 2001;6:613–30.

[11] Cazacu O, Plunkett B, Barlat F. Orthotropic yield criterion for hexagonal close packed metals. Int J Plast 2006;22:1171–94.

[12] Choi SH, Brem JC, Barlat F, Oh KH. Macroscopic anisotropy in AA5019A sheets. Acta Mater 2000;48:1853–63.

[13] Cottrell JA, Hughes TJR, Bazilevs Yuri. Isogeometric analysis, toward integration of CAD and FEA. Wiley; 2009.

[14] Dasappa P, Inal K, Mishra R. The effects of anisotropic yield functions and their material parameters on prediction of forming limit diagrams. Int J Solids Struct 2012;49:3528–50.

[15] Dawson P. Crystal plasticity. In: Continuum Scale Simulation of Engineering Materials Fundamentals Microstructures Process Applications. Raabe D, Roters F, Barlat F, Chen L-Q. (Eds.), Wiley-VCH Verlag GmbH, Berlin, 2004, p. 115–43.

[16] Dodd B, Caddell RM. On the anomalous behaviour of anisotropic sheet metals. Int J Mech Sci 1984;26:113–8.

[17] Esmaeili S, Lloyd DJ, Poole WJ. A yield strength model for the Al-Mg-Si-Cu alloy AA6111. Acta Mater 2003;51:2243–57.

[18] Gambin W. Plasticity and texture. Amsterdam: Kluwer Academic Publishers; 2001.

[19] Hershey AV. The plasticity of an isotropic aggregate of anisotropic face centered cubic crystals. J Appl Mech Trans ASME 1954;21:241.

[20] Hill R. A theory of the yielding and plastic flow of anisotropic metals. Proc R Soc Lond 1948;A193:281.

[21] Hosford WF. A generalized isotropic yield criterion. J Appl Mech Trans ASME 1972;39:607.

[22] Hughes TJR, Cottrel JA, Bazilevs Y. Isogeometric analysis: CAD, finite elements, NURBS, exact geometry and mesh refinement. Comput Methods Appl Mech Eng 2005;194:4135–95.

[23] Karafillis AP, Boyce MC. A general anisotropic yield criterion using bonds and a transformation weighting tensor. J Mech Phys Solids 1993;41:1859–86.

[24] Kocks UF, Tomé CN, Wenk HR. Texture and anisotropy: preferred orientations in polycristals and their effect on material properties. Cambridge University Press; 1998.

[25] Kuroda M, Tvergaard V. Forming limit diagrams for anisotropic metal sheets with different yield criteria. Int J Solids Struct 2000;37:5037–59.

[26] Lebensohn RA, Tome CN. A self-consistent anisotropic approach for the simulation of plastic deformation and texture development of polycrystals: Application to zirconium alloys. Acta Metall Et Mater 1993;41:2611–24.

[27] Lou XY, Li M, Boger RK, Agnew SR, Wagoner RH. Hardening evolution of AZ31B Mg sheet. Int J Plast 2007;23:44–86.

[28] Lou Y, Huh H, Lim S, Pack K. New ductile fracture criterion for prediction of fracture forming limit diagrams of sheet metals. Int J Solids Struct 2012;49:3605–15.

[29] Les Piegl, Wayne Tiller. The NURBS book. Berlin: Springer-Verlag; 1996.

[30] Plunkett B, Lebensohn RA, Cazacu O, Barlat F. Anisotropic yield function of hexagonal materials taking into account texture development and anisotropic hardening. Acta Mater 2006;54:4159–69.

[31] Plunkett B, Cazacu O, Barlat F. Orthotropic yield criteria for description of the anisotropy in tension and compression of sheet metals. Int J Plast 2008;24:847–66.

[32] Proust G, Tome CN, Kaschner GC. Modeling texture, twinning and hardening evolution during deformation of hexagonal materials. Acta Mater 2007;55:2137–48.

[33] Rockafellar RT. Convex analysis. Princeton, NY: Princeton University Press; 1970.

[34] Simo JC, Hughes TJR. Computational inelasticity, interdisciplinary applied mathematics. 7. Springer; 1998.

[35] Soare SC, Benzerga AA. On the modelling of asymmetric yield functions. Int J Solids Struct 2016;80:486–500.

[36] Stoughton TB, Yoon JW. Path independent forming limits in strain and stress spaces. Int J Solids Struct 2012;49:3616–25.

[37] Stoughton TB, Yoon JW. A pressure-sensitive yield criterion under a non-associated flow rule for sheet metal forming. Int J Plast 2004;20:705–31.

[38] von Mises R. Mechanik der festen Körper im plastisch deformablen Zustand. Göttin Nachr Math Phys 1913;1:582–92.

[39] Yang DY, Kim YJ. A rigid-plastic finite element calculation for the analysis of general deformation of planar anisotropic sheet metals and its application. Int J Mech Sci 1986;28:825.

[40] Yoon JW, Song IS, Yang DY, Chung K, Barlat F. Finite element method for sheet forming based on an anisotropic strain-rate potential and the convected coordinate system. Int J Mech Sci 1995;37:733.

[41] Yoon JW, Barlat F, Chung K, Pourboghrat F, Yang DY. Earing predictions based on asymmetric nonquadratic yield function. Int J Plast 2000;16:1075–104.

[42] Yoon JW, Dick RE, Barlat F. A new analytical theory for earing generated from anisotropic plasticity. Int J Plast 2011;27:1165–84.

[43] Yoon JW, Barlat F, Dick RE, Karabin ME. Prediction of six or eight ears in a drawn cup based on a new anisotropic yield function. Int J Plast 2006;22:174–93.